PERGAMON

Corrosion Science 43 (2001) 1781–1791

CORROSION SCIENCE

www.elsevier.com/locate/corsci

Corrosion behavior of advanced titanium-based alloys made by three-dimensional printing (3DP^{TM}) for biomedical applications

S.-B. Hong [a,b], N. Eliaz [c], E.M. Sachs [d], S.M. Allen [b], R.M. Latanision [c,*]

[a] *Harvard School of Dental Medicine, Boston, MA 02115-5888, USA*
[b] *Department of Materials Science and Engineering, Massachusetts Institute of Technology, Cambridge, MA 02139-4307, USA*
[c] *Department of Materials Science and Engineering, H.H. Uhlig Corrosion Laboratory, Massachusetts Institute of Technology, Cambridge, MA 02139-4307, USA*
[d] *Department of Mechanical Engineering, Massachusetts Institute of Technology, Cambridge, MA 02139-4307, USA*

Received 13 September 2000; accepted 8 November 2000

Abstract

New Ti–5Ag and Ti–5Ag–35Sn (wt.%) alloys were designed and synthesized by three-dimensional printing (3DP^{TM}) through liquid-phase sintering or liquid-tin infiltration, respectively. The corrosion behavior of these alloys as well as of pure titanium was studied by means of short- and long-term open-circuit potential and potentiodynamic measurements during immersion in a saline solution at body temperature, as well as by Auger electron spectroscopy (AES). Due to its relatively low porosity level and the presence of silver, the Ti–5Ag alloy sintered at 1300°C exhibited good passivation behavior. However, the Ti–5Ag–35Sn alloy, while exhibiting improved dimensional stability, suffered from a deteriorated corrosion resistance.

Keywords: Ti-based alloys; Three-dimensional printing (3DP^{TM}); Prostheses; Corrosion

* Corresponding author. Tel.: +1-617-253-4697; fax: +1-617-253-8745.
E-mail address: lats@mit.edu (R.M. Latanision).

0010-938X/01/$ - see front matter
PII: S0010-938X(00)00181-5

1. Introduction

Both clinical experience and research on metallic implants have indicated the destructive effects of corrosion in human body. Corrosion affects the performance and durability of the implant device, but it also releases products that may stimulate an unpredicted biological response.

Titanium is the most widely used material for medical implants [1,2]. It is light ($\rho = 4.51\ \mathrm{g\,cm^{-3}}$), biologically and chemically inert, and has low electrical and thermal conductivity ($\sigma = 2.3 \times 10^4\ \Omega^{-1}\,\mathrm{cm^{-1}}$ at 22°C, $\lambda = 22\ \mathrm{W\,m^{-1}\,K^{-1}}$ at 27°C, respectively) in comparison to other metals [3,4]. Titanium does not warm significantly as a result of exposure to the magnetic field involved in magnetic resonance imaging (MRI) testing. In addition, because it has a coefficient of thermal expansion which is similar to that of the bone, MRI testing complications due to thermal expansion and distortion are minimized. Since titanium is weakly paramagnetic, image interference in MRI or computed tomography (CT) scans is not observed [5]. The ability to form surface passive films on titanium, and to retain them under conditions of in vivo service, provides a protective barrier from corrosive environments and characteristics that allow for histological *osseo*integration.

Three-dimensional printing (3DP^{TM}) is a process invented at MIT for the rapid fabrication of three-dimensional parts directly from computer models [6–8]. Fig. 1 shows a schematic of this process, in which a solid object is formed by printing a sequence of two-dimensional layers. The formation of each layer involves the spreading of a thin layer of a powdered material, followed by selective joining of

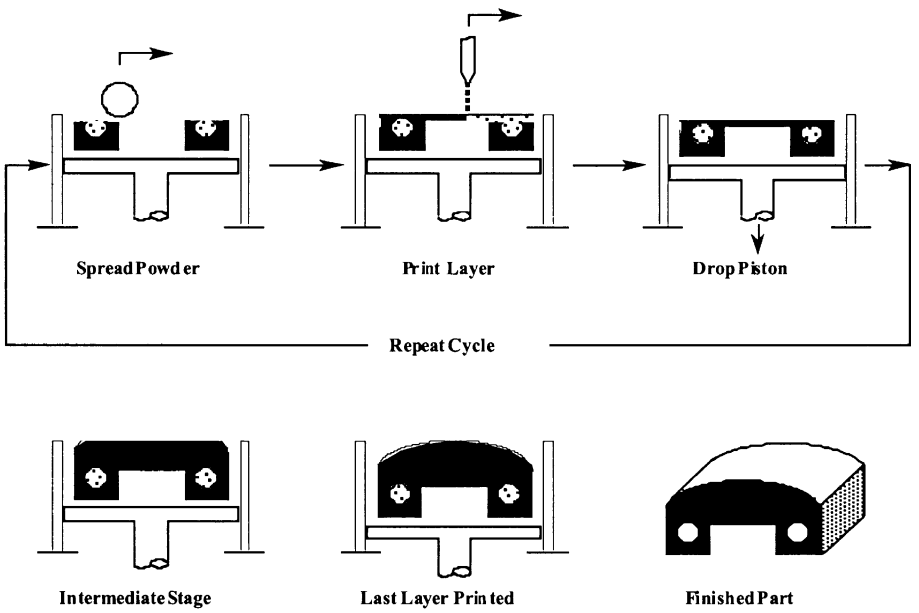

Fig. 1. A schematic of three-dimensional printing (3DP^{TM}) process.

powder through printing of a binder material. Subsequently, the cylinder containing the powder bed is lowered, allowing for the spread of the next layer of powder. Unbound powder temporarily supports unconnected portions of the component, allowing overhangs, undercuts and internal volumes to be formed. The unbound powder is removed upon process completion, leaving the finished green part.

3DP™ offers several significant advantages over other processes for customized fabrication of prostheses. First, it can form parts of almost any geometry; e.g., structures with complex geometry and/or small dimensions can be produced with significantly more precision. In addition, it can be scaled-up both in size and rate through the use of multiple nozzle printheads on a raster machine, and is adaptable to different material systems.

In spite of these promising advantages, suitable material systems that exhibit the vital combination of strength and biocompatibility have yet to be identified. Thus, the objective of this work was to study the corrosion behavior of advanced Ti-based alloys, designed and synthesized by 3DP™, with respect to their potential use for biomedical applications.

2. Experimental details

Two types of alloys were designed and synthesized in the framework of this work – Ti–5Ag made through liquid-phase sintering, and Ti–5Ag–35Sn made through liquid-tin infiltration. A detailed description of design criteria and synthesis procedures is given elsewhere [9].

In brief, due to its good sinterability and flowability, spherical atomized pure titanium powder was selected as feedstock for the titanium alloys. The commercial powder (99.9% pure, Surepure Chemetals, Florham Park, NJ) size was 60 ± 15 μm in diameter. Binders are used in 3DP™ to selectively join the powder particles together during printing [10]. Four different wax- and acrylic polymer-based binders were shown to introduce carbon contamination into the final sintered part [9]. To avoid this problem, inorganic reactive binders were selected for use. Because silver exhibits high solubility and diffusivity in titanium as well as acceptable biocompatibility, two aqueous silver salt solutions were examined as potential binders. While silver carbonate (Ag_2CO_3) was shown to provide insufficient binding of the titanium particles, a solution of silver nitrate ($AgNO_3$) worked well and was used in this work. A 5.8 M aqueous solution of $AgNO_3$ (Alfa Aesar, Ward Hill, MA) was deposited as droplets into a titanium powder bed. The powder bed was subsequently heated for 1 h at 450°C under argon gas atmosphere in an alumina tube furnace. Under such conditions, silver is reduced to form rigid necks between titanium powder particles. The mechanical integrity of the sintered block material was evaluated by verifying that it was undamaged after being placed in an ultrasonic bath (GT-120, LECO, St. Joseph, MI) for a few minutes. The block material was then machined into thin samples with large square faces.

Full densification of the printed material was achieved through either a final sintering stage (Ti–5Ag) or liquid-tin infiltration (Ti–5Ag–35Sn). In the first case, the

thin samples were sintered in a vacuum furnace at two different temperatures (1150°C or 1300°C). Alumina powder bed encapsulation was used both to protect the samples against oxidation and to reduce the temperature gradient around them. A heating rate of 8°C min^{-1} was employed up to 700°C, followed by heating at 2°C min^{-1} up to the maximum sintering temperature, at which the samples were kept for 1 h. Upon completion of the final sintering stage, the number of pores and their size were measured by analyzing environmental scanning electron microscope (XL30 ESEM-FEG, Philips, Eindhoven, Holland) micrographs with an image analysis software package (NIH Image 1.62, NIH, Bethesda, MD), following a standard procedure [11]. The porosity (i.e., the volume fraction of pores) was found to increase with decreasing sintering temperature (Fig. 2(a) and (b), Table 1).

In the case of liquid-tin infiltration, the printed Ti–Ag material was infiltrated with tin at 700°C under argon gas atmosphere. ESEM and X-ray diffraction (XRD) observations revealed the presence of pure titanium particles surrounded by thin layers of the Ti–7Ag–61Sn and Ti–67Sn (Ti_6Sn_5) phases. Typical microstructure of the infiltrated alloy is shown in Fig. 2(c). Some Ti–Ag–Sn samples were further homogenized at 750°C for 10 h under vacuum. The microstructure of the infiltrated and homogenized alloy (Fig. 2(d)) was consisted of the Ti–67Sn (Ti_6Sn_5) and Ti–57Sn (Ti_2Sn) phases.

The corrosion behavior of the fully densified alloys, as well as of pure titanium control samples, was characterized. The control samples were cut from a 3.175 mm thick plate (Alfa Aesar, Ward Hill, MA), formed by a sequence of hot rolling, cold

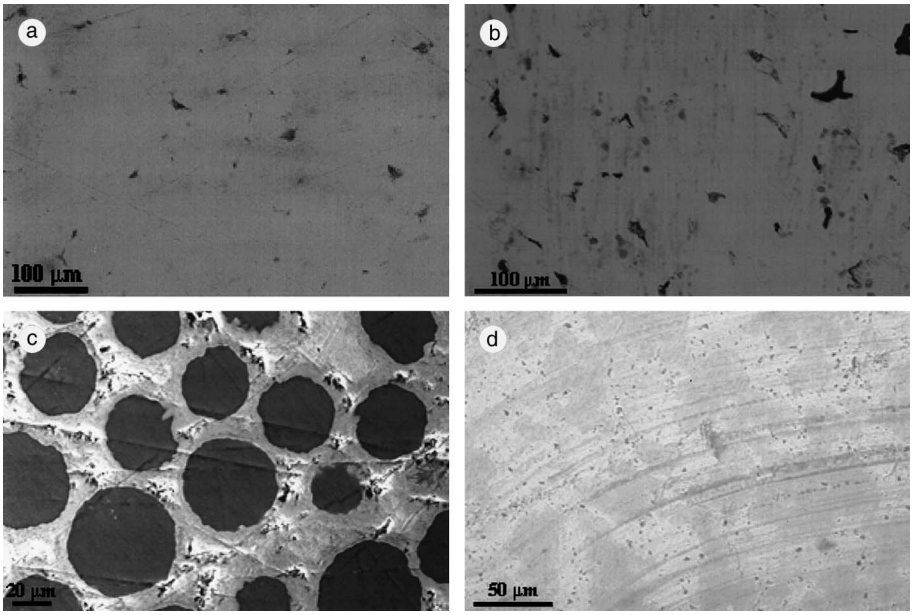

Fig. 2. Back scattered electron images of Ti–5Ag alloys sintered at: (a) 1300°C, and (b) 1150°C. Secondary electron images of: (c) infiltrated, and (d) infiltrated and homogenized Ti–Ag–Sn alloys.

Table 1
Porosity and corrosion measurements of Ti–5Ag and Ti–5Ag–35Sn (wt.%) alloys. The equivalent values for pure titanium are shown for comparison

Sample	Fabrication	Porosity[a]	E_{corr}[b] (mV)	i_{corr}[c] ($A\,cm^{-2}$)
Pure Ti[d]	Rolling and annealing	~0	-380 ± 42	$(1.3 \pm 0.3) \times 10^{-7}$
Ti–5Ag	Sintered at 1300°C[e]	1.50 ± 0.73	-210 ± 35	$(7.8 \pm 0.2) \times 10^{-7}$
Ti–5Ag	Sintered at 1150°C[e]	6.30 ± 3.30	-230 ± 31	$(8.9 \pm 0.5) \times 10^{-7}$
Ti–5Ag–35Sn	Sn-infiltrated	<0.8	-500 ± 37	$(5.3 \pm 1.7) \times 10^{-6}$
Ti–5Ag–35Sn	Sn-infiltrated and homogenized	<0.8	-530 ± 49	$(4.6 \pm 1.9) \times 10^{-6}$

[a] In percent. The mean and standard deviation were obtained by analyzing SEM micrographs with an image analysis software package, taking into account seven fields in each sample.
[b] Vs. SCE ($n = 4$).
[c] The corrosion current density obtained from the potentiodynamic curve generated during the first hour of immersion in saline solution ($n = 4$).
[d] Control sample (plate).
[e] Heating rate: $2°C\,min^{-1}$.

rolling and annealing operations. Electrochemical measurements were carried out on specimens with an exposed area of approximately 1×1 cm^2. Both open-circuit potential and potentiodynamic measurements were carried out on four specimens to ensure repeatability. Each specimen was prepared in three steps. First, a copper wire was attached to the sample by both a silver paint and 5 Minute® epoxy. A glass tube was epoxied to the sample to prevent exposure of the wire to the electrolyte. Next, the sample was mounted in a cold mount resin. Finally, after curing, the specimen was ground with 600 grit grinding paper. A standard three-electrode system was used for the electrochemical measurements, with saturated calomel electrode (SCE) as the reference electrode, and pure platinum foil as the counter electrode. A non-deaerated saline solution (0.9% NaCl, pH 5.5), maintained at body temperature (~37°C), was used as the electrolyte. The open-circuit potential (E_{OCP}) was monitored for 20 min using an electrochemical interface (Model SI 1286, Schlumberger, Hampshire, England). Subsequently, potentiodynamic measurements were carried out at a scan rate of 1.0 $mV\,s^{-1}$ from −200 mV vs. E_{OCP} to +1500 mV vs. SCE. The corrosion current density was determined through extrapolation of the cathodic polarization curve (potentiodynamic measurement).

To assess the long-term stability of the surface passive layer, another set of measurements was carried out, in which E_{OCP} was monitored for 20 days, while samples as those described before were kept at 37°C. Finally, Auger electron spectroscopy (AES) depth profiles were obtained for pure titanium control samples and Ti–5Ag samples sintered at 1300°C, before and after 20 days immersion. For this purpose, samples were cut into 5×2 mm^2 pieces and ground with 600 grit grinding paper. After being dried in a desiccator at room temperature, the samples were Argon-ion sputtered at 2.0 kV and 10 $mA\,cm^{-2}$. The chemical composition of the surface was scanned at 1 min intervals until the oxygen level significantly decreased. Then, the samples were immersed in a saline solution at 37°C for 20 days. Subsequently, AES experiments were repeated to identify any changes in either chemical composition or thickness of the oxide layer.

3. Results

Fig. 3 shows typical potentiodynamic curves for each of the five materials. From this figure it is evident that the curves for the pure titanium control sample and for the Ti–Ag alloy sintered at 1300°C are similar in shape, although the Ti–Ag alloy exhibits a less active corrosion potential (E_{corr}). The Ti–Ag alloy sintered at 1150°C, however, exhibits a less stable passivation (or metastable pitting) at high potentials. With regard to corrosion current density (i_{corr}), the Ti–Ag alloys sintered at either 1300°C or 1150°C exhibited higher values compared to the titanium control samples, although of the same order of magnitude (Table 1). From Fig. 3 it is also evident that the corrosion potential is much more active, and the corrosion current density is higher, for the Ti–Ag–Sn alloys, either in the as-infiltrated or in the infiltrated and homogenized conditions. Values of E_{corr} and i_{corr} typical for the different materials are summarized in Table 1.

Fig. 4 shows the typical time dependence of the open-circuit potential of all five materials during long-term (20 days) immersion in a saline solution at 37°C. During the first week of immersion, E_{OCP} of pure Ti and the Ti–Ag alloy sintered at 1300°C increased (i.e., became more noble) with time. After one week, a steady state was attained in both cases. Over the whole 20 day period, the Ti–5Ag alloy sintered at 1300°C exhibited the less negative E_{OCP} among all five materials. The E_{OCP} of the Ti–Ag alloy sintered at 1150°C as well as of the Ti–Ag–Sn alloys did not show a similar distinct increase with increasing immersion period.

Fig. 5 shows AES depth profiles for pure Ti and Ti–Ag alloy sintered at 1300°C, before and after 20 days of immersion in a saline solution at 37°C. The sputtering time is proportional to the depth of removed material. However, the exact thickness of surface layer could not be determined in the absence of a titanium oxide standard of known thickness. Yet, the AES depth profiles indicate a slight increase in the thickness of the oxide on pure Ti, but no increase in the thickness of the oxide on Ti–Ag sintered at 1300°C. Furthermore, the outer layer of the oxide on the Ti–Ag alloy became significantly enriched with oxygen as a result of immersion.

4. Discussion

The dominant cathodic reaction in the non-deaerated saline solution can be estimated on the basis of the corrosion potentials measured for the different materials (Table 1). From the Nernst equation for the hydrogen evolution reaction

$$E_{H^+/H_2} = E^0_{H^+/H_2} - 0.059\text{pH} \quad (1)$$

E_{H^+/H_2} is approximately −0.57 V vs. SCE at pH 5.5. Because none of the samples exhibited a corrosion potential which was more negative than −0.57 V vs. SCE, hydrogen reduction was probably not a major cathodic reaction in this study.

Fig. 3 shows a similar shape of potentiodynamic curves for pure titanium and the Ti–5Ag alloys. The corrosion potential of both Ti–5Ag alloys is higher than that of

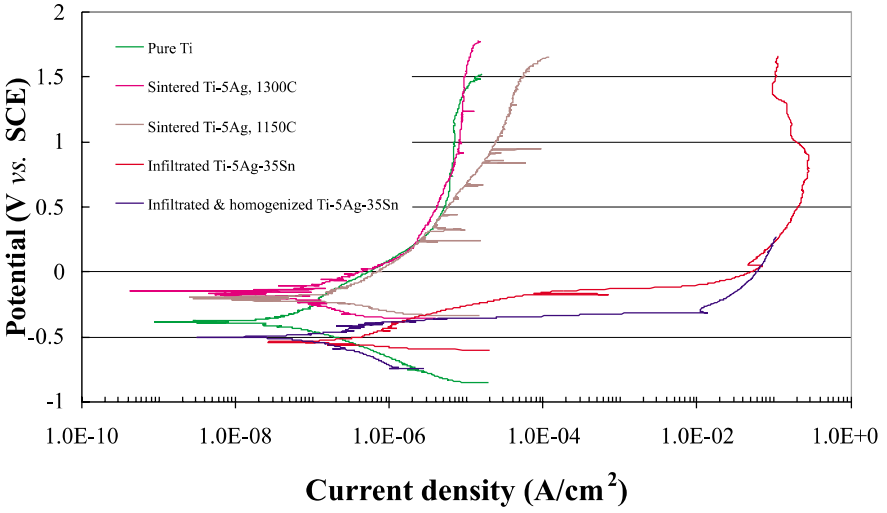

Fig. 3. Typical contours of potentiodynamic curves for the studied materials.

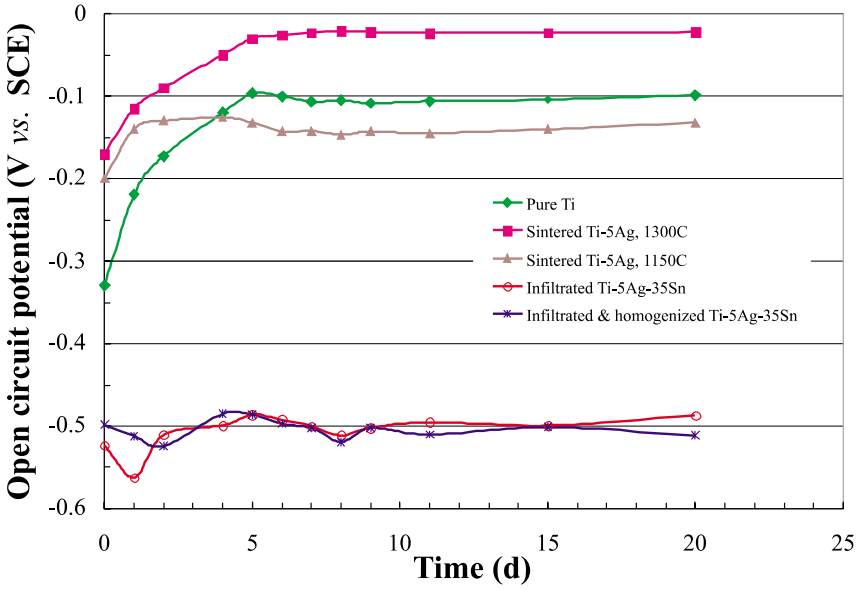

Fig. 4. Time dependence of the open-circuit potential of the studied materials.

the pure titanium metal, as also evident from the long-term monitoring of E_{OCP} (Fig. 4). Fig. 4, however, shows that the E_{OCP} of the Ti–5Ag alloy sintered at 1150°C becomes smaller than the E_{OCP} of pure titanium after almost four days of immersion in saline solution. In principal, the Ti–Ag system may represent galvanic coupling between a passive metal and a noble metal. Typically, coupling of titanium with

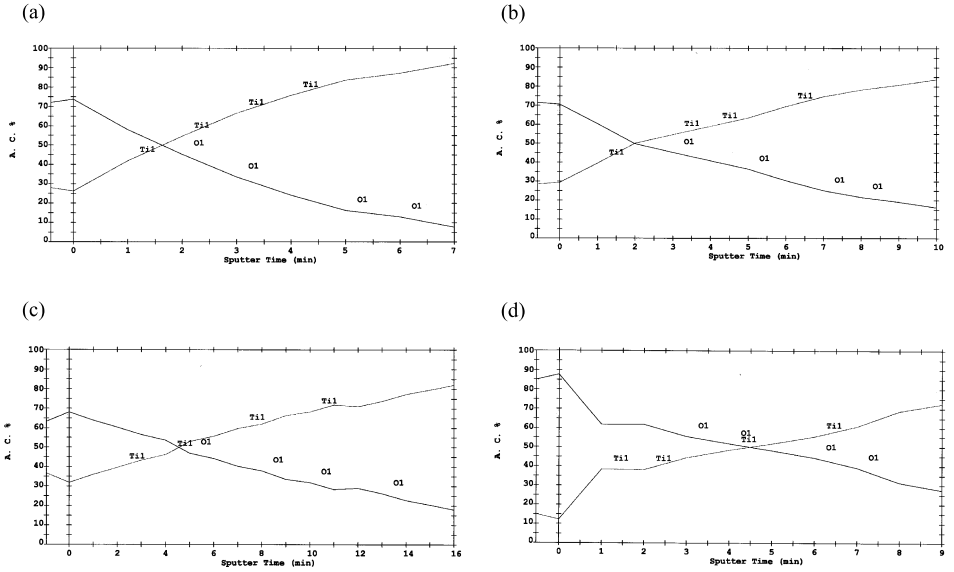

Fig. 5. Auger electron spectroscopy depth profiles before and after 20 days of immersion in a saline solution at 37°C: (a) pure Ti before immersion, (b) pure Ti after immersion, (c) Ti–Ag sintered at 1300°C before immersion, and (d) Ti–Ag sintered at 1300°C after immersion.

noble metals such as platinum, gold, or palladium results in spontaneous passivation, since these noble metals act as good catalysts (i.e., have higher exchange current densities, i_0) for the hydrogen and oxygen reduction (cathodic) reactions. The presence of 5 wt.% Ag (standard reduction potential, $E^0_{Ag} = 0.799$ V vs. SHE) may thus be enough to raise the corrosion potential of the Ti–Ag system. Because sintering at 1300°C results in a more chemical homogeneity in comparison to sintering at 1150°C, the mentioned effect of silver on the corrosion potential is more significant for the former alloy. It should be noted that a non-deaerated solution was used for this study. If the solution was deaerated, however, the combination of a more significant contribution of the hydrogen reduction reaction and a corrosion potential increase due to the presence of Ag could have stabilized the Ti–Ag system in the passive region. Thus, the positive effect of adding silver, in terms of corrosion behavior, could have become even more distinct.

In terms of corrosion current density, the values for both Ti–5Ag alloys were higher than that for pure titanium (Table 1). This difference can be explained in terms of the real surface area in contact with the electrolyte. The porosity in both Ti–5Ag alloys makes the real surface area larger, thus increasing the corrosion current density. Furthermore, because the Ti–5Ag alloy sintered at 1150°C has more as well as bigger pores on the surface, localized breakdown of the passive layer is evident from its potentiodynamic curve (Fig. 3). It is well known that for high-porosity compact samples, the morphology of surface porosity (e.g., open channels), as well as the size and number of pores, affect the occurrence of localized corrosion [12].

Ti–Ag–Sn alloys also exhibit a galvanic couple behavior. However, this behavior is much different from the one observed for the Ti–Ag system, as evident from the different shape of potentiodynamic curves in both cases (Fig. 3). At a constant potential, the cathodic polarization curve of Sn typically exhibits a lower current density, while the anodic polarization curve of Sn exhibits a much higher current density, compared to Ti [13]. Therefore, the corrosion potential is likely determined by Sn anodic reaction and Ti cathodic reaction. Consequently, the Ti–Ag–Sn alloys do not exhibit any passivation before the dissolution of tin is significantly increased.

From long-term open-circuit potential measurements (Fig. 4), both the pure Ti control sample and the Ti–5Ag alloys exhibited an increased E_{OCP} with increasing time. Because the oxygen reduction rate on a titanium surface is much lower compared to any other oxidizers, about a week may be required for the reduction reaction to attain steady state. Silver seems to have no significant effect on the kinetics of steady state passivation, as the difference between E_{OCP} values for pure titanium and for the Ti–5Ag alloy sintered at 1300°C remained approximately constant over the 20-day immersion period. The addition of Sn, however, affects the kinetics of attaining steady state passivation.

From the Pourbaix diagram for the Ti–water system at 25°C [14] it is evident that titanium hydroxide, $Ti(OH)_3$, or titanium oxide, TiO_2, are expected to be thermodynamically stable under conditions of pH 5.5 and non-deaerated solution. The natural passive film formed on titanium when exposed to different synthetic physiological solutions is typically a few nanometers thick, and contains a relatively high concentration of oxygen vacancies. The titanium oxide layer may be described as an *n*-type semiconductor containing anion vacancies (Fig. 6) [13]. It is known that the kinetics of titanium corrosion in neutral solutions is controlled by migration of oxygen vacancies across the oxide film. Thus, a thick TiO_2 film containing a low

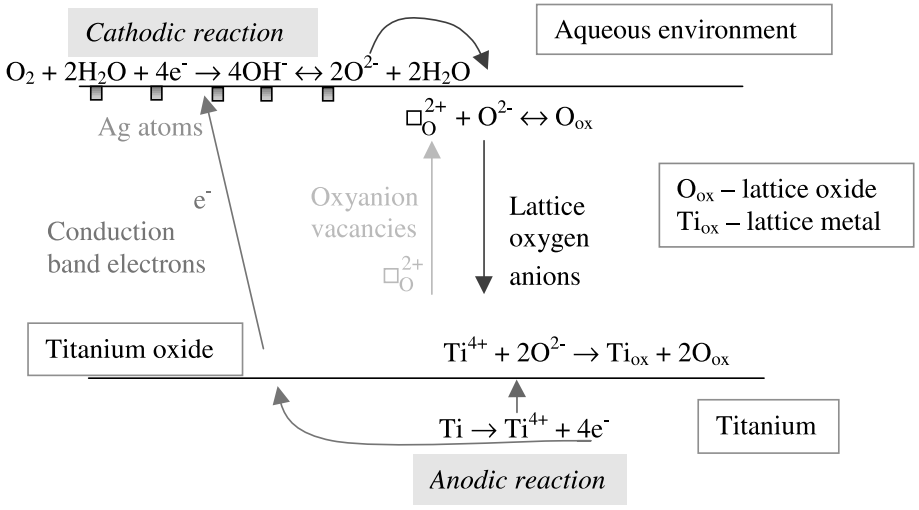

Fig. 6. Processes across an *n*-type anion vacancy titanium oxide film.

concentration of oxygen vacancies will lead to a very slow mass transport rate across the film [15]. It is also anticipated that the basic oxidation reaction would usually take place at the oxide/metal interface following oxygen anions migration [16].

On the basis of the aforementioned model for an *n*-type titanium oxide layer and AES results for pure titanium control samples and Ti–5Ag alloy sintered at 1300°C (Fig. 5), the increase in E_{OCP} with increasing immersion time may be related to a decrease in the passivation current density. With regard to pure titanium, as the surface oxide layer becomes thicker, the kinetics of mass transport through the layer becomes slower, thus resulting in a decrease in the passivation current density. On the other hand, silver enhances the oxygen anion uptake in the oxide layer on Ti–5Ag alloy, thus consuming oxygen anion vacancies. This vacancy deficit may result in a reduced passivation current density.

5. Conclusions

In this study, new Ti–5Ag and Ti–5Ag–35Sn alloys were designed and synthesized by 3DP™ through liquid-phase sintering or liquid-tin infiltration, respectively. Based on results of in vitro electrochemical measurements and surface analysis, while comparing to results for pure titanium control samples, the following conclusions were drawn:

1. Due to its relatively low porosity level and the presence of Ag, Ti–5Ag alloy made by 3DP™ and sintering at 1300°C exhibits good passivation behavior in an environment simulating body conditions. On the other hand, Ti–5Ag alloy made by 3DP™ and sintering at 1150°C shows inferior corrosion behavior due to higher porosity level and a less homogeneous distribution of silver.
2. Tin infiltration, while improving the dimensional stability of the material, deteriorates its corrosion resistance. Therefore, it does not seem a promising approach for the fabrication of titanium-based prostheses.
3. Ti–5Ag alloy made by 3DP™ and sintering at 1300°C seems to be a good candidate for the customized fabrication of prostheses. Thus, cell culture and/or animal studies should further be carried out to confirm biocompatibility.

Acknowledgements

This work was supported by the 3DP™ group at MIT and made use of MRSEC shared facilities supported by the National Science Foundation under award number DMR-9400334.

References

[1] B.A. Toth, D.S. Ellis, W.B. Stewart, Plast. Reconstr. Surg. 81 (1988) 315.
[2] C.L. Chandler, D. Uttley, D.J. Archer, D. Mac Vicar, Br. J. Neurosurg. 8 (1994) 409.

[3] D. Simpson, Neurosurgery 26 (1990) 361.
[4] C. Kittel, Introduction to Solid State Physics, seventh ed., Wiley, New York, 1996, pp. 126, 160.
[5] P.K. Sullivan, J.F. Smith, A.A. Rozzelle, Plast. Reconstr. Surg. 94 (1994) 589.
[6] E. Sachs, J. Haggerty, P. Williams, M. Cima, Three-Dimensional Printing Techniques, US Patent 5,204,055, April 20, 1993.
[7] E. Sachs, M. Cima, P. Williams, D. Brancazio, J. Cornie, J. Engng. Indust. 114 (4) (1992) 481.
[8] E. Sachs, M. Cima, J. Bredt, A. Curodeau, Manufact. Rev. 5 (2) (1992) 118.
[9] S.B. Hong, Individualized cranio-maxillo-facial prosthesis construction using three-dimensional printing (3DP^{TM}) with atomized titanium powder, Ph.D. Thesis, Harvard School of Dental Medicine, Boston, MA, 2000.
[10] H. Guo, Alloy design for three-dimensional printing of hardenable tool materials, Ph.D. Thesis, Massachusetts Institute of Technology, Cambridge, MA, 1998.
[11] ASTM E 1245 – 95, Standard practice for determining the inclusion or second-phase constituent content of metals by automatic image analysis, 1999 Annual Book of ASTM Standards, vol. 03.01, American Society for Testing and Materials, West Conshohocken, PA, 1999.
[12] K.H.W. Seah, R. Thampuran, X. Chen, S.H. Teoh, Corros. Sci. 37 (9) (1995) 1333.
[13] D.A. Jones, Principles and Prevention of Corrosion, Macmillan, New York, 1992, p. 184, pp. 411–416.
[14] J. Schmets, J. van Muylder, M. Pourbaix, in: M. Pourbaix (Ed.), Atlas of Electrochemical Equilibria in Aqueous Solutions, NACE, Houston, TX, 1974, pp. 213–222.
[15] J. Pan, C. Leygraf, D. Thierry, A.M. Ektessabi, J. Biomedical, Mater. Res. 35 (1997) 309.
[16] N. Birks, G.H. Meier, Introduction to High-Temperature Oxidation of Metals, Arnold, London, 1983, pp. 32–62.